



## Original Article

# Dynamic assessment of the seismic isolation influence for various aircraft impact loads on the CPR1000 containment



Runyu Mei <sup>a, b</sup>, Jianbo Li <sup>a, b, \*</sup>, Gao Lin <sup>a, b</sup>, Xiuyun Zhu <sup>c</sup>

<sup>a</sup> State Key Laboratory of Coastal and Offshore Engineering, Dalian University of Technology, Dalian 116024, China

<sup>c</sup> Plant Site and Civil Engineering Department, Nuclear and Radiation Safety Center, Ministry of Environmental Protection of PRC, Beijing, 100082, China

## article info

### Article history:

Received 25 April 2018

Received in revised form

29 July 2018

Accepted 4 August 2018

Available online 6 August 2018

### Keywords:

CPR1000 containment

Seismic isolation bearing

Aircraft impact

Dynamic behavior

## abstract

An aircraft impact (AI) on a nuclear power plant (NPP) is considered to be a beyond-design-basis event that draws considerable attention in the nuclear field. As some NPPs have already adopted the seismic isolation technology, and there are relevant standards to guide the application of this technology in future NPPs, a new challenge is that nuclear power engineers have to determine a reasonable method for performing AI analysis of base-isolated NPPs. Hence, dynamic influences of the seismic isolation on the vibration and structural damage characteristics of the base-isolated CPR1000 containment are studied under various aircraft loads. Unlike the seismic case, the impact energy of AI is directly impacting on the superstructure. Under the coupled influence of the seismic isolation and the various AI load, the flexible isolation layer weakens the constraint function of the foundation on the superstructure, the results show that the seismic isolation bearings will produce a large horizontal deformation if the AI load is large enough, the acceleration response at the base-mat will also be significantly affected by the different horizontal stiffness of the isolation bearing. These concerns require consideration during the design of the seismic isolation system.

© 2018 Korean Nuclear Society. Published by Elsevier Korea LLC. This is an open access article under the CC BY-NC-ND license (<http://creativecommons.org/licenses/by-nc-nd/4.0/>).

## 1. Introduction

In the event of an extreme accident, such as an earthquake, a large fire, or an aircraft impact (AI), the safety and integrity of nuclear power plants (NPPs) should be ensured, and the release of radioactive materials should be precluded. Since the 9/11 incident, the United States has promulgated several regulations, such as [1] and has decided that the design of new NPPs must be evaluated against hostile impacts from large-scale commercial aircraft. The research pertaining to AIs on NPPs was initiated by Ref. [2]. The following scholars' research is mainly from the following research perspectives: the global structural damage, local structural damage, and effects of fuel-initiated fires, as well as the functional failure of the structures, systems, and components (SSCs) due to the induced vibrations in the structural members and safety related equipment [3].

[4] used the force-time history method and missile-target interaction method to analyze the vibration characteristic of the NPP under an impact by a 747-400 aircraft, and the sensitivity of the results on the assumed Riera force-loading area was evaluated. [5] analyzed the impact of the tendon prestressing, impact angle, and impact position on the impact load and dynamic response of the containment. [6] conducted a safety assessment of an A92 reactor building under a Boeing 747 impact by analyzing different parameters through a multistep process. [7] conducted a comprehensive review of the AI analyses of nuclear-safety-related concrete structures. [8] appraised the vibration safety of the internal equipment and components in the primary auxiliary buildings. [9] and [10] analyzed the influence of an induced fire from an AI on the outer containment of an NPP. [11] and [12] have done a study of the mechanical properties of reactor pressure vessels under thermal shock, which can be applied to the thermal stress analysis induced by a fire caused by AI. In an AI evaluation, the NPP is often assumed to be a structure without a seismic isolation system, and the boundary conditions are generally considered to be fixed boundaries.

The previous nuclear accidents caused by strong earthquakes, such as the Kashiwazaki Kariwa nuclear accident in July 2007 and the Fukushima nuclear accident in March 2011, have directly led to

<sup>b</sup> Institute of Earthquake Engineering, Dalian University of Technology, Dalian 116024, Liaoning, China

\* Corresponding author. No.2 Linggong Road, Ganjingzi District, Dalian City, Liaoning Province, China.

E-mail address: [jianboli@dlut.edu.cn](mailto:jianboli@dlut.edu.cn) (J. Li).

a substantial increase in the current seismic fortification standards for NPPs. Thus, the NPP designers doubt the aseismic capabilities of traditional earthquake resistance measures. Seismic isolation is proven as an effective technology for reducing the seismic response of a superstructure from its base to negotiate the destructive ground movement. The guidance for the seismic isolation of NPPs is presently available in ASCE4-16 and other relevant standards. Seismic isolation has been deployed in the NPPs of France and South Africa, thus, generating a new concern regarding the impact analysis of an aircraft on a base-isolated NPP. [13] noted that an NRC-funded research project studied the topic of AI analyses for seismically isolated nuclear structures and stated that the safety of the isolated structures under an AI should be evaluated. Currently, there is little research pertaining to this aspect of AI analyses.

For an NPP with a seismic isolation system, the flexible isolation layer weakens the constraint function of the foundation to the superstructure. The seismic energy that is transmitted from the underground region to the superstructure is weakened by isolator, shown in Fig. 1(a). Unlike the seismic load case, the aircraft load case consists of a short-duration impact occurring in a single arbitrary direction in space on superstructure, shown in Fig. 1(b). The impact energy is directly acting on the superstructure. Under the impact of such loads, the influence of isolation bearings on the dynamic behavior of NPPs is needed to be studied, such as the local damage of the containment and the vibration response of the NPPs.

In this study, the dynamic characteristics of the base-isolated CPR1000 containment under AI are analyzed, and based on these results, a reasonable analysis model is proposed. This paper is organized into the following sections. Section 2 establishes a representative detailed three-dimensional (3D) model of the CPR1000 containment. A series of six isolation bearings are selected, and the isolation performance of each isolation bearing is analyzed and verified in Section 3. An AI containment analysis is conducted with the six isolation bearings. In Section 4, based on the 3D finite element (FE) model of the containment, three different AI loads are considered. The distributions of the concrete plastic strain, displacement response of the containment, and acceleration response of the containment are analyzed. Finally, the conclusions are presented in Section 5.

## 2. Geometric and 3D FE modeling of the containment

### 2.1. Geometric modeling of the containment

The structure of the CPR1000 pressurized water reactor is

illustrated in Fig. 2 and is mainly composed of three parts: the concrete containment, steel lining, and prestressed reinforcement. The concrete containment includes the base mat, cylinder, and dome. The inner diameter of the containment is 37 m, the height of the cylinder is 50.11 m, the total height from the bottom of the plate to the dome is 66.68 m, the normal thickness of the dome is 0.8 m, and the normal wall thickness of the cylinder is 0.9 m. Two layers of the circumferential and vertical prestressed reinforcement are shown in Fig. 4 and Fig. 5, respectively. The upper end of the vertical prestressed reinforcement is anchored at the top surface of the ring beam, and the lower end is anchored to the base mat of the containment. In addition, three layers of prestressed reinforcement, which are anchored on the ring beam, are arranged in the dome. The inner side of the concrete containment structure is also connected with a layer of 6 mm thick steel lining, which is connected to the concrete containment with rivets.

### 2.2. FE modeling of the containment

#### 2.2.1. Concrete constitutive model

When conducting a structural dynamic analysis, a proper and reliable model that can reflect the concrete material behavior at high strain rates is needed. [15] used the Winfrith concrete model to simulate the impact resistance of steel-plate concrete and reinforced concrete panels. [16] used the plasticity concrete model to simulate an AI on the concrete containment. [8] evaluated the vibration safety of the primary auxiliary buildings using the CSMC concrete model. In this study, the plasticity concrete model is selected. This model includes the damage and strain rate effects and has been widely used for modeling concrete members subject

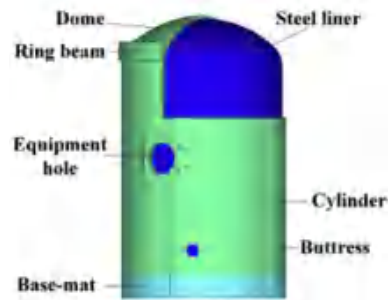


Fig. 2. CPR1000 containment.

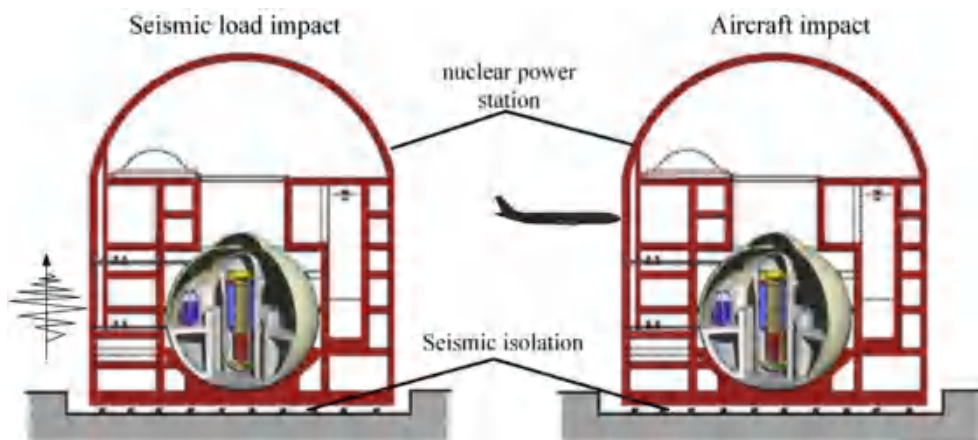


Fig. 1. The schematic diagram of an NPP with seismic isolation under a seismic load and AI.

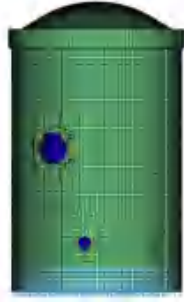


Fig. 3. FE model of the CPR1000 containment.



Fig. 4. Positive view of the prestressed reinforcement.

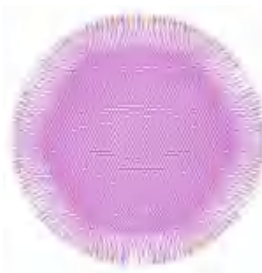


Fig. 5. Top view of the prestressed reinforcement.

to high-velocity impacts, such as projectile perforation, reinforced concrete targets, and AI on a concrete containment.

This concrete model decouples the volumetric and deviatoric responses of concrete. The volumetric response is easily captured via a tabulated input which gives the current pressure as a function of current and previous minimum (most compressive) volumetric strain. A three-failure-surface model is used to analyze deviatoric responses, as shown in Fig. 6. During initial loading or reloading, the deviatoric stresses remain elastic until the stress reaches the initial yield surface. The deviatoric stresses can then further increase until the maximum yield surface is reached. Beyond this stage the response can be perfectly plastic or soften to the residual yield surface [17].  $a_{0y}$ ,  $a_{1y}$ ,  $a_{2y}$ ,  $a_0$ ,  $a_1$ ,  $a_2$ ,  $a_{1f}$ ,  $a_{2f}$  are material constants. Mean stress  $P = -(S_1 + S_2 + S_3)/3$ .  $S_1$ ,  $S_2$ ,  $S_3$  are the first, second and third principal stresses respectively.

$$DS_y = a_{0y} + \frac{P}{a_{1y} + a_{2y}} \text{ (initial yield surface);} \quad (1)$$

$$DS_m = a_0 + \frac{P}{a_1 + a_2} \text{ (maximum yield surface);} \quad (2)$$

$$DS_r = \frac{P}{a_{1f} + a_{2f}} \text{ (residual yield surface);} \quad (3)$$

In Eq. (4), after reaching the initial yield surface but before the maximum failure surface, the current surface  $DS_f$  is obtained as a linear interpolation between  $DS_m$  and  $DS_y$ . In Eq. (5), after reaching the maximum surface the current failure surface  $DS_h$  is similarly interpolated between  $DS_m$  and  $DS_r$ . The function  $h(l)$  varies from 0 to 1 depending on the accumulated effective plastic strain parameter  $l$ . This function would normally begin at 0 at  $l = 0$ , increase to 1 at some value  $l = l_m$ , and then decrease to 0 at some larger value of  $l$ .  $l_m$  is defined simply as the value of  $l$  corresponding to the first relative maximum of  $h$ . Based on this, the elasticity, plasticity and softening deformation of concrete can be qualitatively described.

$$DS_f = h DS_m + (1 - h) DS_y; \quad (4)$$

and

$$DS_h = h DS_m + (1 - h) DS_r; \quad (5)$$

The main advantage of this model is that one user input is required, the unconfined compressive strength. Other parameters are automatically generated within the program. The required concrete parameters include the density ( $\rho = 2500 \text{ kg/m}^3$ ), Poisson's ratio ( $\nu = 0.2$ ); uniaxial compressive strength ( $f_c = 41 \text{ MPa}$ ), and uniaxial tensile strength ( $f_t = 2.85 \text{ MPa}$ ) [18].

To consider the strain rate effect of concrete, a dynamic increase factor (DIF) is introduced in this study. The DIF represents the ratio of the dynamic-to-static strength versus the strain rate. The DIF of the compressive strength for CEB is given in Eq. (6) and Eq. (7) [19,20].

$$CDIF = \frac{f_{cd}}{f_{cs}} = \left( \frac{\dot{\epsilon}_d}{\dot{\epsilon}_{cs}} \right)^{1.026a} \dot{\epsilon}_d \leq 30 \text{ s}^{-1} \quad (6)$$

and

$$CDIF = \frac{f_{cd}}{f_{cs}} = g(\dot{\epsilon}_d)^{1=3} \dot{\epsilon}_d > 30 \text{ s}^{-1}; \quad (7)$$

where  $f_{cd}$  is the dynamic compressive strength at the strain rate  $\dot{\epsilon}_d$ ;  $f_{cs}$  is the static compressive strength at strain rate  $\dot{\epsilon}_{cs}$  ( $\dot{\epsilon}_{cs} = 30 \times 10^{-6} \text{ s}^{-1}$ );  $g = 6.156a - 0.49$  and  $a = (5 + 3f_{cu})^{-1}$ ;  $f_{cu}$  is the static compressive strength.

The DIF of concrete the tensile strength is determined by Eq. (8) and Eq. (9).

$$TDIF = \frac{f_{td}}{f_{ts}} = \left( \frac{\dot{\epsilon}_d}{\dot{\epsilon}_{ts}} \right)^d \dot{\epsilon}_d \leq 1 \text{ s}^{-1} \quad (8)$$

and

$$TDIF = \frac{f_{td}}{f_{ts}} = b \left( \frac{\dot{\epsilon}_d}{\dot{\epsilon}_s} \right)^{1=3} \dot{\epsilon}_d \geq 1 \text{ s}^{-1}; \quad (9)$$

where  $f_{td}$  is the dynamic tensile strength at the strain rate  $\dot{\epsilon}_d$ ;  $f_{ts}$  is the static tensile strength at the strain rate  $\dot{\epsilon}_{ts}$  ( $\dot{\epsilon}_{ts} = 1$ );  $b = 6d - 2$ ,  $d = 1 = 1 + 8f_c^{'} / f_{co}^{''}$ ; and  $f_{co}^{''} = 10 \text{ MPa}$ ;  $f_c^{''}$  is the static tensile strength.

This constitutive model was used in the latest LS-DYNA software code [14], corresponding to keyword card Mat\_Concrete\_Damage\_Rel3.

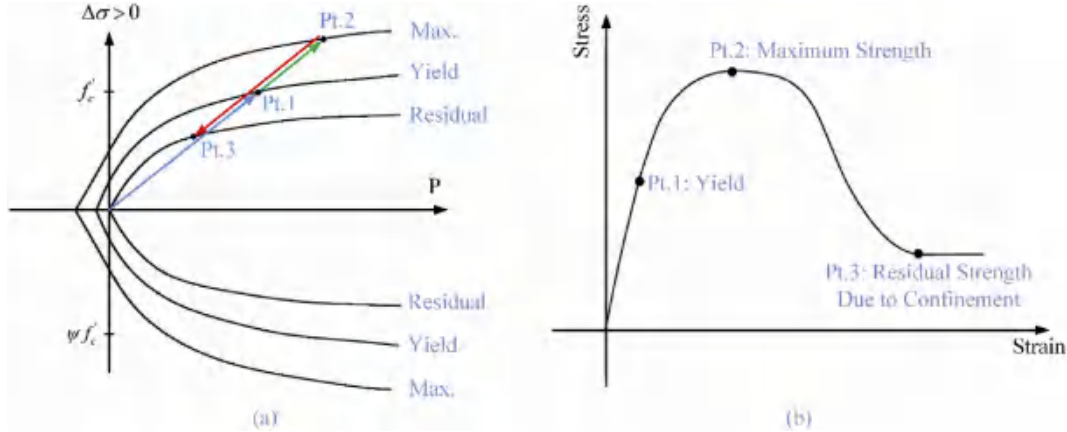


Fig. 6. Strength model for concrete, (a) failure surface of the concrete material model and uniaxial stress-strain relationship.

### 2.2.2. Metal structural model

Fig. 7 shows the elastic-plastic model with the kinematic hardening material model that is used to model the behavior of the prestressed reinforcement and steel lining. In this paper, kinematic hardening of the metal was considered by setting the parameter  $b = 0$ . The prestressed reinforcement is embedded in the concrete using the option \*CONSTRAINED\_LAGRANGE\_IN\_SOLID. This method does not require the consideration of complex reinforcement modeling problems, while maintaining good accuracy and stability. The steel lining and concrete structure are closely connected by rivets. The steel liner is simulated by shell elements with six degrees of freedom per node, and the concrete is simulated by solid elements with three degrees of freedom per node. Considering the difference in the nodal degrees of freedom for the two elements, the keyword \*CONTACT\_TIED\_NODES\_TO\_SURFACE is used to simulate the close connection between the steel lining and concrete surface.

In this study, the yield strength of the rebar and structural steel is highly dependent upon the strain rate. The yield strength increases when the strain rate increases. This dynamic yield strength of steel is taken into consideration by the CowpereSymonds formula for uniaxial tension or compression, as shown in Eq. (10).

$$\frac{S_d}{S_y} = 1 + \left( \frac{\dot{\epsilon}}{C} \right)^{\frac{1}{P}}; \quad (10)$$

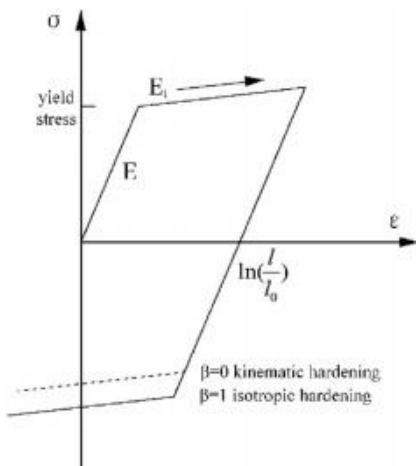


Fig. 7. The kinematic hardening material model.

where  $S_d$  is the dynamic yield strength;  $S_y$  is the static yield strength;  $\dot{\epsilon}$  is the strain rate;  $C$  and  $P$  are the constants of the CowpereSymonds relation. The material parameters of the prestressed reinforcement and steel lining are presented in Table 1 [21].

### 2.2.3. Summary of the FE containment model

According to the above analysis, the detailed FE model, shown in Fig. 3, is established by using the ANSYS16.0/LS-DYNA software [14]. The main components of the containment are simulated. The concrete is simulated by solid164 with multilayered solid elements along the radial direction; the steel lining is simulated by shell163; the prestressed reinforcement is simulated by link160, and the prestress load is added by applying an initial stress to the link element [22].

In order to verify the rationality of this concrete constitutive model, metal structural model and the corresponding material parameters, such as the  $C$  and  $P$  of the steel bar, the impact tests of a 1/7.5 ratio GE J79 engine with 215 m/s impact velocity on 12 cm thick reinforced concrete target plate conducted by Muto in 1989 [23] are simulated. The FE model of the engine and reinforced concrete target plate are shown in Fig. 8. The coupling interaction between steel bar and concrete in reinforced concrete plate adopts the keyword of \*CONSTRAINED\_LAGRANGE\_IN\_SOLID. Both the material model of steel bar and engine adopt the Plastic Kinematic model. Lastly, 304,164 elements are used for the entire model. The size of the impact hole obtained by numerical simulation is 198 mm  $\times$  208 mm, which is very close to the experimental result 185 mm  $\times$  195 mm, shown in Fig. 9. The residual velocity of the engine after perforate the panel is also very close to the experimental result 54 m/s, shown in Fig. 10. From the comparison results, the reinforcement coupling method used in the CPR1000 finite element model and the selected concrete and reinforcement material constitutive model and the corresponding material parameters are reasonable.

### 3. Seismic isolators

At present, there are several types of new and existing isolation

Table 1  
Material parameters of the metal structure.

	$\Gamma(\text{kg}=\text{m}^3)$	$E/\text{Pa}$	$n$	$S_y/\text{Pa}$	$C$	$P$
Prestressed reinforcement	7850	1.9e11	0.3	1.77e8	641	7.3
Steel lining	7850	2.06e11	0.3	3.25e8	40.4	5

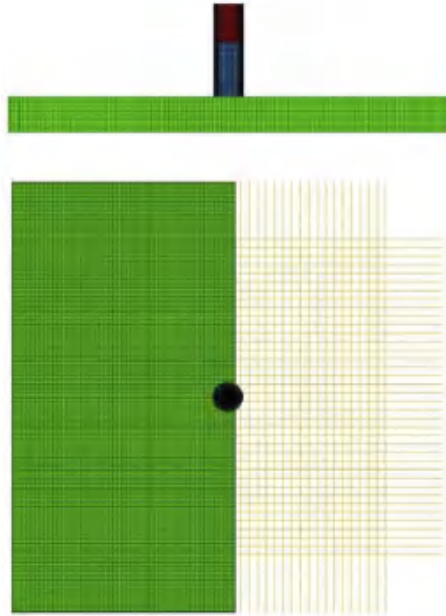


Fig. 8. The FE model used in the engine impact tests.

systems, such as the low damping rubber bearing (LDRB), lead rubber bearing (LRB), friction sliding isolator (FSI), high damping rubber bearing (HDRB), and friction pendulum isolator. For elastomeric bearings, the behavior of the LDRB, LRB, and HDRB in shear is well established [24,25]. The mathematical model of the shear behavior for these bearings can be simplified into a bilinear restoring force model, as shown in Fig. 11. However, the damping characteristics of these isolating bearings are considerably different. For the LDRB, owing to its low viscous damping, additional damping should be added during the design and construction to improve the damping effect. The HDRB uses a rubber with a high damping property. The LRB mainly relies on the lead core to exert the damping effect of the bearing. When the dynamic analysis is conducted, the damping of the isolation bearing affects the dynamic characteristics of the structure, especially under an AI.

This work does not involve the study and design of the isolation bearings for the CPR1000 containment according to the relevant

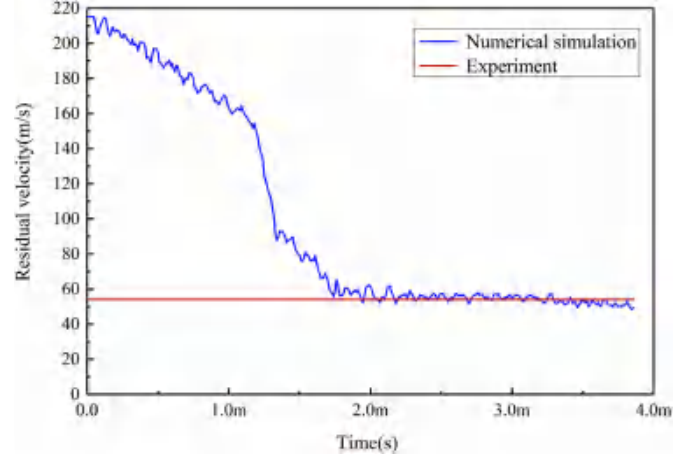


Fig. 10. The comparison of engine residual velocity between numerical results and experimental results.

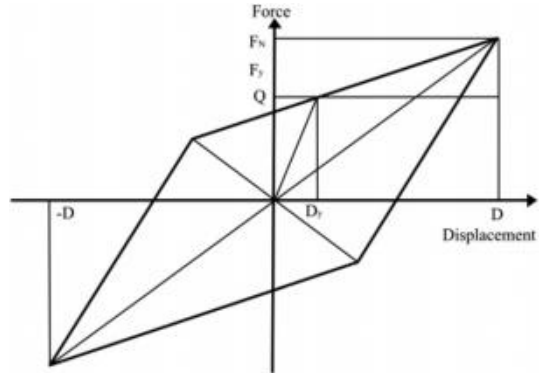


Fig. 11. Bilinear restoring force model.

specifications; this study is a qualitative analysis of the influence of the isolation bearings on the dynamic behavior of the CPR1000 containment under different AI loads. The influence of the isolation bearings on the horizontal stiffness is mainly considered, and the additional damping is assumed to be small. In the LS-DYNA code, the isolators can be modeled by a linear spring

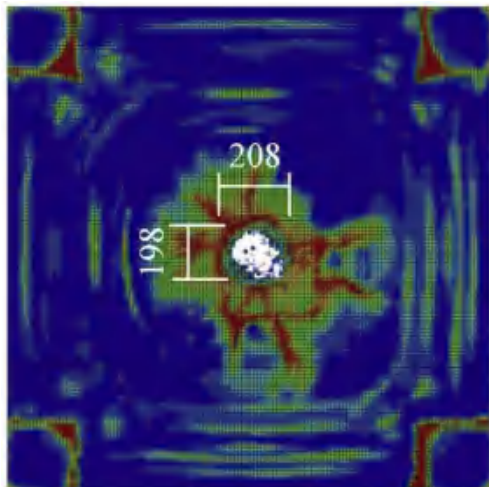
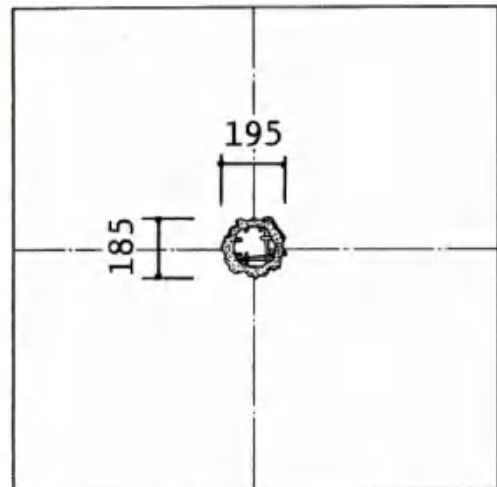


Fig. 9. Comparison of the damage of front face of panel between numerical results and experimental results (units: mm).



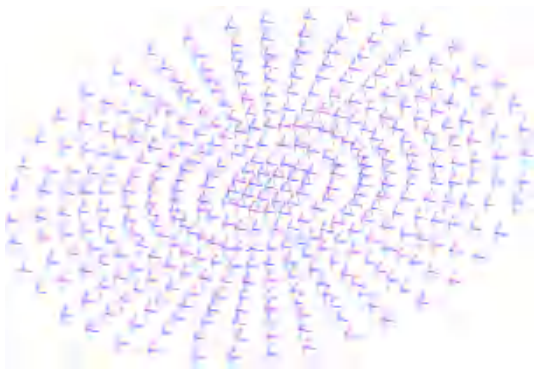


Fig. 12. Layout of the isolators.

Table 2  
Various cases for the isolation bearings.

Parameter	Unit	case 1	case 2	case 3	case 4	case 5	case 6
Design load	kN	706	1256	1963	2827	3848	6361
Equivalent stiffness	kN/m	882	1325	1480	1859	2531	2841
Pre-yielding stiffness	kN/m	3091	4647	5187	6519	8873	9959
Post-yielding stiffness	kN/m	476	715	798	1003	1365	1532
Yield force	kN	23.6	41.9	65.4	94.2	128.2	212
$T_e$	mm	58	68.6	96	110	110	162

Table 3  
Natural frequency (Hz).

Mode no.	Case						
	case 1	case 2	case 3	case 4	case 5	case 6	case 7
1	0.71	0.89	0.94	1.05	1.21	1.30	4.09
2	0.72	0.89	0.94	1.05	1.21	1.30	4.13
3	0.90	1.10	1.13	1.29	1.44	1.58	6.39

(\*MAT\_SPRING\_ELASTIC) in the vertical direction and nonlinear spring (\*MAT\_SPRING\_ELASTOPLASTIC) and viscous damper (\*MAT\_DAMPER\_VISCOUS) in horizontal directions, as shown in Fig. 12.

Tensile deformation in elastomeric bearings has traditionally been considered undesirable. In the preliminary analysis, the vertical deformation analysis of the isolation bearing under AI is carried out (The AI loads will be introduced in section 4). And the

analysis result shows that the isolation bearings are entirely experienced compression deformation. [24,25] summed up the important conclusions of other scholars' experimental work on the tensile properties of elastomeric bearings. One of them shows the load-deformation behavior in tension is linear up to cavitation with the tensile stiffness approximately equal to the compressive stiffness, followed by nonlinear post-cavitation behavior. So, the vertical tension stiffness coefficient of the isolation bearing is considered to be the same as the compression stiffness coefficient.

Lastly, a series of six different isolation bearings are determined by trial calculation. However, prior to the AI analysis, the isolation performance of the selected isolation bearings is analyzed. Thus, combined with the non-isolation condition, seven different boundary conditions are composed. The six different isolation bearings are represented by case 1 through case 6, and the material parameters of these isolation bearings are given in Table 2. Case 7 represents the non-isolation condition.

### 3.1. Seismic analysis

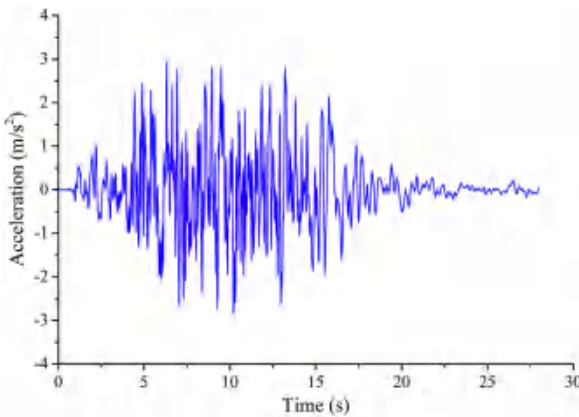
For superstructures, the target of the design is to reach "seismic isolation" by designing the stiffness and damping of the isolation layer to reasonably extend the first period of structure, to dissipate the seismic energy, and to moderately control the displacement of the isolation layer. Generally, the structure mostly moves in the horizontal plane with rigid body behavior under seismic loads [26,27,28]. To a certain extent, the motion of the base mat can reflect not only the motion of the whole structure, but also the deformation of the isolation bearings. The decreasing amplitude ratio (DAR) can reflect the decreasing function of the superstructure response under earthquake excitation.

$$\text{DAR} = \left| \frac{S_a - S_b}{S_b} \right|; \quad (11)$$

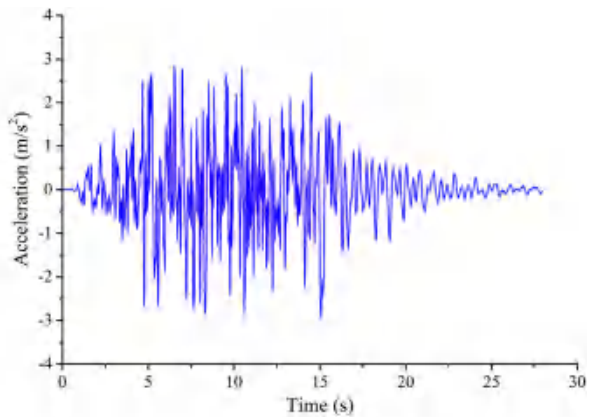
where DAR is the decreasing amplitude ratio;  $S_a$  is the response of the non-isolated structure;  $S_b$  is the response of the isolated structure.

Lastly, the maximum resultant horizontal displacements of the base-mat and DARs of the dome vertex for the above seven cases are analyzed and compared.

After generating the 3D FE models of the main structures, the modal and seismic analyses are conducted for case 1 through case 7. Table 3 presents the modal results, which indicate that the



(a)



(b)

Fig. 13. Acceleration time histories of RG1.60 in each direction (a) X and (b) Y.

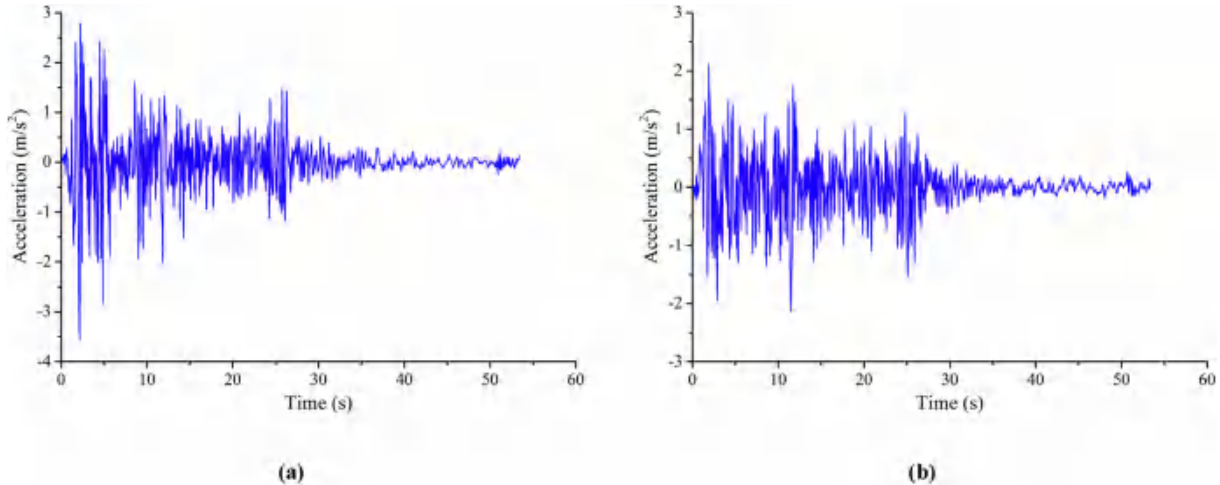


Fig. 14. Acceleration time histories of El Centro in the direction (a) X and (b) Y.

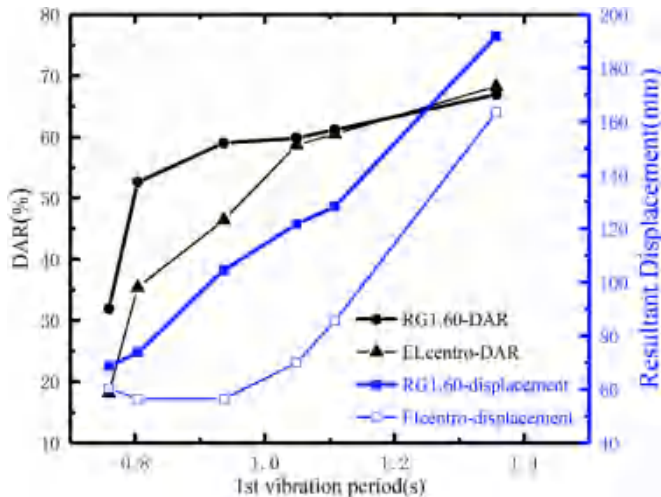


Fig. 15. The DAR and the maximum resultant horizontal displacement of the containment under different seismic loads.

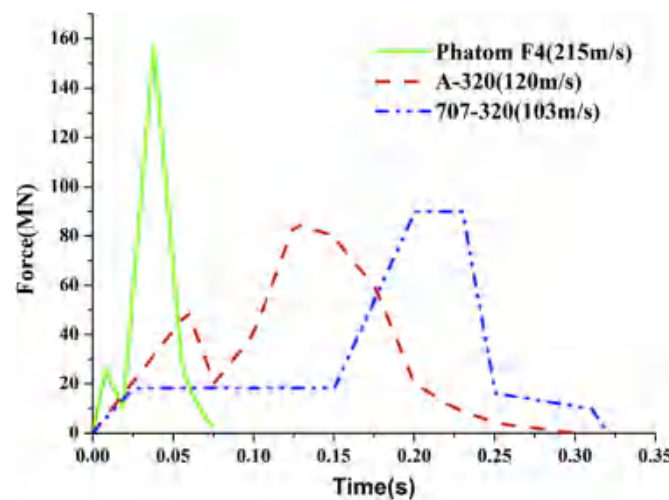


Fig. 16. Reaction time response of the aircrafts.



Fig. 17. Impact location and direction.

vibration frequency of the structure is associated with the horizontal stiffness of the isolation bearings.

For the seismic analysis, two types of seismic waves are considered as the seismic oscillation input. Additionally, only the effects of horizontal earthquakes are considered. One seismic oscillation input is the artificial seismic wave derived from the Regulatory Guide 1.60 reference response spectra (RG1.60), as shown in Fig. 13. The peak ground acceleration for the X and Y directions is equal to 0.3 g. The other seismic oscillation input is the El Centro seismic wave, as shown in Fig. 14.

Based on the numerical results, the maximum resultant displacements of the base mat and DAR of the dome vertex for each case under these two seismic loads are shown in Fig. 15. The lateral axis in the diagram represents the first vibration period for each case. Considering these two types of seismic loads, the variation of the DAR and the maximum resultant horizontal displacement are similar. From case 1 to case 6, the DAR and maximum resultant horizontal displacement will increase with an increase in the vibration period. The growth rate of the DAR slowly decreases, while the maximum resultant horizontal displacement demonstrates the opposite trend.

One of the isolation system design criteria requires that the

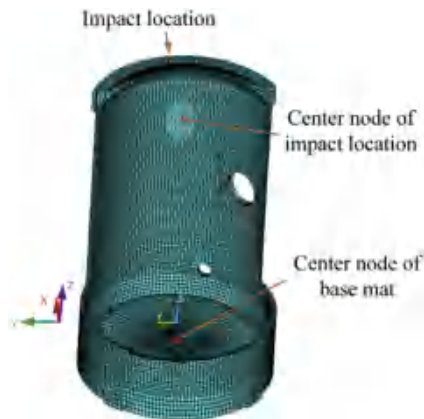


Fig. 18. The reference points of the CPR1000.

calculated horizontal maximum resultant displacement of the isolated structure must remain less than 3 Te (Te is the total thickness of the rubber, presented in Table 2). For case 1, the DAR

under RG1.60 excitation is 66.93%, and 68.27% under El Centro excitation; the maximum resultant horizontal displacement is 191.95 mm under RG1.60 excitation exceeding 3 Te, 163.59 mm under El Centro excitation. The maximum resultant horizontal displacements from case 2 through case 6 do not exceed 3 Te, thus, meeting the relevant requirements. For case 6, the DAR reaches 18.14% under El Centro excitation, which indicates that the isolation bearing corresponding to this case does not have good isolation performance.

#### 4. Numerical simulation and analysis of an AI on the containment

There are several different characteristics to consider for an AI on an NPP. The plane has complicated deformation and failure mechanisms, the impact area varies in size and shape with respect to time, and the impact load varies with respect to time. Presently, there are two main analytical methods that can currently be implemented for an AI analysis: the force-time history analysis method and missile-target interaction analysis method. The former only needs to specify the impact area and the impact time

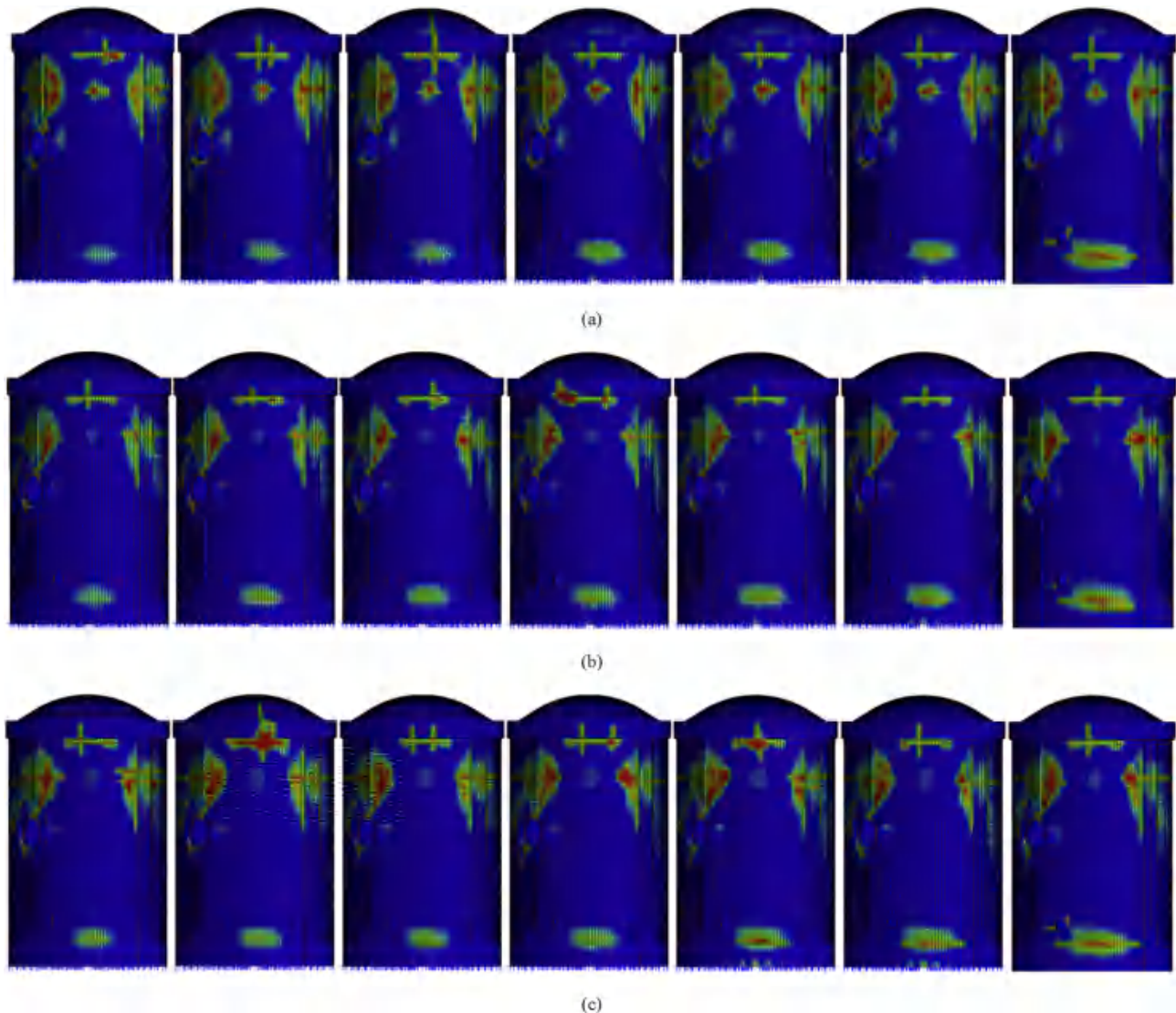


Fig. 19. The plastic strain distribution of the containment under each aircraft load (a) F4, (b) A320, and (c) 707-320.

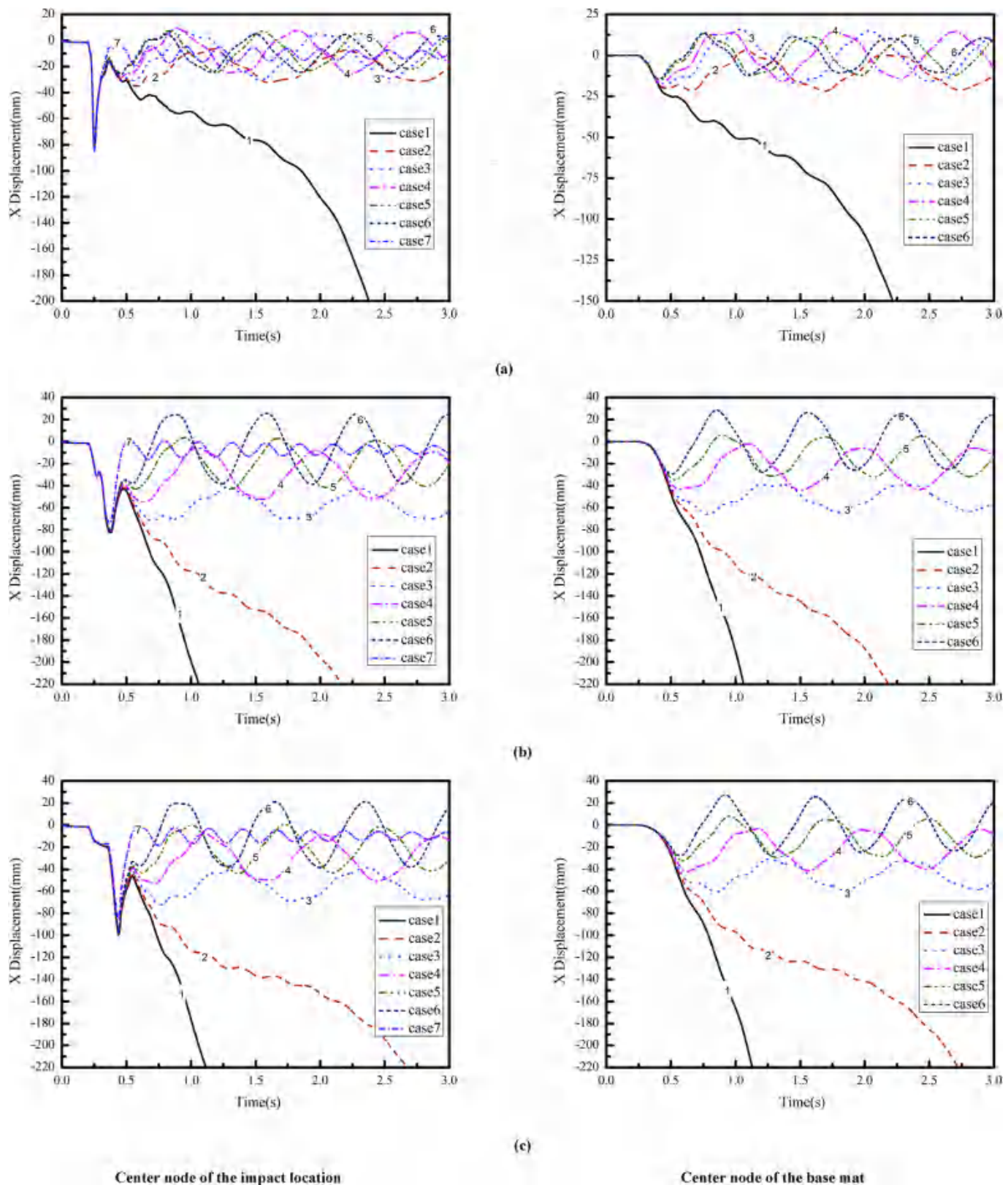


Fig. 20. The X displacement response of the center node of the impact location and the center node of the base mat under the impact of each aircraft load (a) F4, (b) A320, and (c) 707-320.

Table 4

The maximum X displacement of the center node of the impact location during the aircraft impact process (mm).

	case 1	case 2	case 3	case 4	case 5	case 6	case 7
F4	-83.746	-83.559	-83.811	-83.891	-83.679	-83.922	-85.122
A320	-82.595	-81.444	-81.748	-81.34	-80.436	-80.093	-73.608
707-320	-99.372	-100.42	-98.622	-97.172	-101.54	-96.207	-84.89

history load and does not need to build a complex three-dimensional finite element model, so that the analysis efficiency is greatly improved. The accuracy and reliability of the results generated by this method are sensitive to the loading area and timing of load application. [29] noted that the loading surface of the AI will influence the deflection, damaged area, and reaction force of the slab.

There are two main approaches to consider for calculating the impact area. One divides the impact area into three regions: the fuselage, wing, and engine [30]. The other simplifies the impact area into a circular area [31–34]. M.R. Sadique and Mohd. Ashraf Iqbal considered that when the purpose is to evaluate the global response of the containment, simplifications can be made for the determination of contact area. They analyzed the impact area of Phantom F4 (215 m/s), Airbus A-320 (120 m/s) and Boeing 707-320 (103 m/s) is a circular area of 6 in diameter, Boeing 747-400 (120 m/s) and Boeing 767-400 (120 m/s) is a circular area of 12 in diameter.

Taking into account the characteristics of different AI loads, fighter Phantom F4 (215 m/s), commercial aircraft Airbus A-320 (120 m/s), and Boeing 707-320 (103 m/s) are selected, which are referred to as F4, 707-320, and A320, respectively, shown in Fig. 16. For each of the aircraft loads, the impact area is assumed to be circular with a diameter of 6 m. One impact location is considered, which is most critical location located at the junction of the dome and cylinder [33], as shown in Fig. 17. The impact direction is also shown in Fig. 17.

Recent research on AIs has mainly focused on the deformation, destruction, and vibration of NPPs during the aircraft collision. However, relatively little research concerning the dynamic response of the structure in the free attenuation vibration process has been conducted. During this process, the vibration characteristics of a base-isolated NPP are likely to be different from those of a non-isolated structure. The isolation bearings play a major role in the attenuation of the vibration response.

Based on the results of a trial calculation, the calculation time of the entire process is fixed at 3.0 s. The initial 0.2 s is the stable stage of the prestressed reinforcement with large damping. The time range of 0.2 s–3.0 s is for the dynamic calculation process, which is the main consideration of this analysis. This main portion of the analysis contains two processes: the AI process and vibration attenuation process. The influence of the isolation bearings on the dynamic behavior of the containment is analyzed and compared by the distribution of the ultimate plastic strain distribution and vibration response of the containment.

#### 4.1. The plastic strain distribution of the concrete containment

Fig. 19 shows the plastic strain distribution of the containment under various aircraft load. The plastic strain distribution for each aircraft is found to be mainly located on the cylinder positioned on both sides of the impact location, at the medial region of the buttress, and on a portion of the buttress. The ring beam and buttress strengthen the overall stability of the containment, and thus, the distribution of the plastic strain is not dispersed to other portions of the cylinder. Regarding the isolated structure, each aircraft load produces a similar plastic strain region distribution.

Given the stable construction of the containment, which consists of the prestressed reinforcement, cylinder, buttress, ring beam, and steel lining, the AI can damage the structure within the vicinity of the impact area, but the entire structure cannot be damaged.

Under the AI loads, the structure will not incur serious damage if the stiffness is sufficiently high. The AI directly acts on the superstructure over a short duration of time, and therefore, the seismic isolation system is unable to influence the plastic strain distribution of the containment. Consequently, the possibility of excessive displacement and acceleration responses may cause internal equipment failure.

#### 4.2. Dynamic deformation analysis and results

In the analysis of the local damage characteristics of the containment, the deformation of the impact zone requires consideration. The maximum displacement of the center node of the impact location (in Fig. 18) during the AI process is analyzed, as shown in Fig. 20. Owing to the high rigidity and integrity of the base mat, the horizontal displacement of the base mat is considered consistent. Thus, the displacement response of the base mat can be used to effectively analyze the real motion of the containment and to reflect the deformation of the isolation bearings.

The maximum displacements for the seven cases are presented in Table 4. The maximum displacement of the isolated structure is approximately -83.7 mm under the F4 aircraft load, -81.0 mm under the A320 aircraft load, and -99.0 mm under the 707-320 aircraft load. It can be seen from Fig. 20 that during the AI process, the maximum deformation of the rubber bearing does not exceed 50 mm under these three kinds of aircraft loads. The isolation bearings mainly affect the structural response of the free attenuation vibration process and do not produce a notable effect on the response during AI process.

As previously mentioned, the additional damping of the

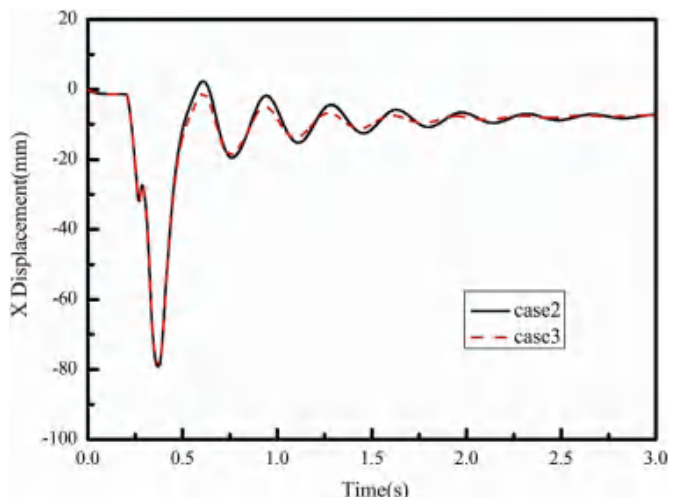


Fig. 21. The X displacement response of the center node of the impact location under the A320 aircraft load for case 2 and case 3 with high damping.

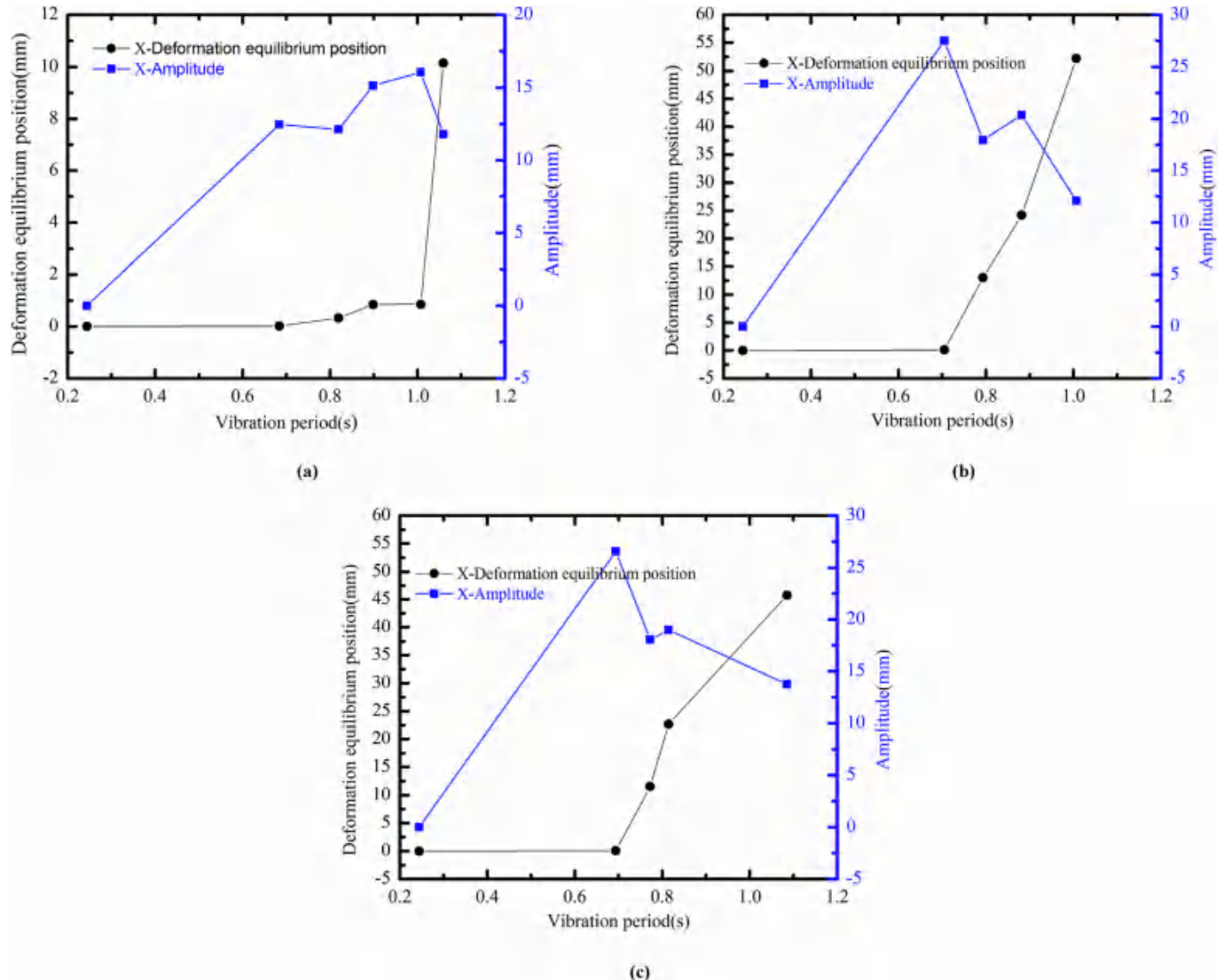


Fig. 22. The vibration characteristics of the containment during the vibration attenuation process under the impact of each aircraft load (a) F4, (b) A320, and (c) 707-320.

isolation bearings will affect the vibration response of the containment. To verify this phenomenon, case 2 and case 3 are considered; the additional damping coefficient is set to  $7 \times 10^6$  N·s·m, and the A320 AI load is adopted. The X displacement responses for the center node of the impact location are similar for these two cases, as shown in Fig. 21. Compared with the results of the vibration attenuation process shown in Fig. 20, the influence of high damping causes the containment to stabilize quickly. Highly damped isolation bearings can quickly consume the kinetic energy produced by the AI. The dynamic behavior of the base-isolated containment under an AI is affected by the horizontal stiffness and damping of the seismic isolation system.

During the vibration attenuation process, there is no external impact force on the containment. A comparison between the displacement response of the central node of the impact location and displacement response of the base mat shows that there is no significant difference after a certain period. Owing to the existence of the seismic isolation system, rigid body motion behavior is demonstrated, acting under its own inertia.

Fig. 20 illustrates the vibrational time history curves of the base-

mat oscillating around an equilibrium position with decreasing amplitude. Thus, under the AI, the yielding of the isolation bearings causes the containment to deviate around its original position. For some situations, such as case 1 under the F4, A320, and 707-320 impacts and case 2 under the A320 and 707-320 impacts, a large horizontal displacement occurs. For these cases, it is possible that the horizontal bearing capacity of the isolation bearings is not able to tolerate the impact of the aircraft.

Excluding these cases, the curves between the first and second peaks for the other cases are selected during the vibration attenuation process. The deformation equilibrium position and amplitude of the base mat in the selected time under different aircraft loads are shown in Fig. 22. The abscissas in the graph represent the time interval of the selection, which is similar to the first vibration period of the containment. Fig. 22 shows that the amplitudes of the containment remain within a small range for the different cases, not exceeding 30 mm. Fig. 22 demonstrates that the deformation equilibrium position does not significantly change prior to a certain vibration period. However, when this vibration period is exceeded, there is a significant increase in the deformation equilibrium

position with an increase in the vibration period. The threshold of the vibration period is reached for case 3 under the F4 load, case 6 under the A320 load, and case 6 under the 707-320 load. Thus, a larger aircraft causes a greater impact, leading to a greater plastic deformation of the isolation bearings.

Owing to the difference in the AI energy and horizontal stiffness of the isolation bearings, different isolation bearings can considerably influence the containment displacement response. In combination with the previous seismic analysis, the deformation of the isolation bearings is more vulnerable to the AI loads. Case 2 has good isolation performance to a certain extent, but under the A320 and 707-320 aircraft loads, the stability and safety of the structure cannot be ensured. As larger AI loads than those considered herein can occur, the influence of these two related factors must be comprehensively considered when selecting the appropriate isolation bearing.

#### 4.3. Floor response spectrum under the AI loads

The seismic response spectrum of the superstructure can be reduced by the isolation bearing system. Under the AI impact loads, the nuclear structure intensely vibrates, and the vibration intensity weakens with increasing distance from the impact position. [35] conducted a vibration analysis of a reinforced concrete primary

auxiliary building under a Boeing 767-400 impact and determined that the vibration safety of the structure is not ensured. The induced vibration response is dominated by high-frequency components, and NEI 07-13 Rev. 8 specifies that the acceleration response spectrum of the nuclear power equipment under an AI is to filter out the frequencies above 200 Hz [36]. From the above displacement responses for the central node of the impact location, the vibration responses for these two processes are quite different, and thus, the differences in the results between these two processes require further investigation. There are a few pieces of essential equipment that are connected to the base mat, such as the reactor and steam generator, and therefore, the vibration response of the base mat will impact the safe use of these devices.

From Fig. 23, before the 50 Hz frequency for the different AI loads, there is little difference between the acceleration response spectra for the center node of the impact location among the different cases. In the high-frequency region (frequencies larger than 50 Hz), there are variations in the acceleration response spectra. Considering the results of Fig. 23, the peaks of the acceleration time history from case 1 through case 7 are near  $450 \text{ m/s}^2$  under the F4 load,  $100 \text{ m/s}^2$  under the A320 load, and  $150 \text{ m/s}^2$  under the 707-320 load, and therefore, the largest acceleration response occurs under the F4 load. Thus, a small fighter jet with a high impact speed, like the F4, is capable of producing very large

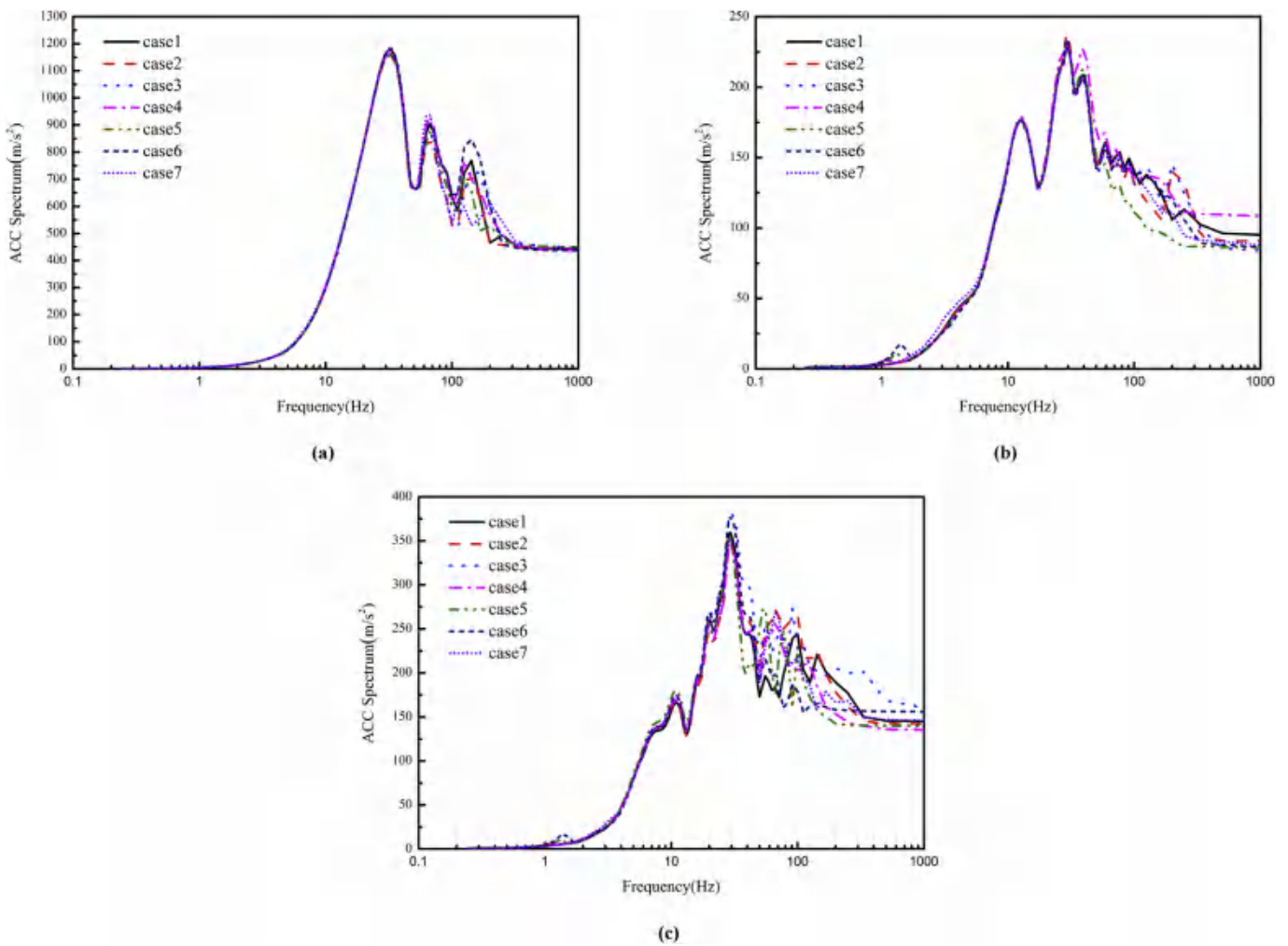


Fig. 23. The X acceleration spectra for the center node of the impact location under each of the AI loads for the whole process: (a) F4, (b) A320, and (c) 707-320.

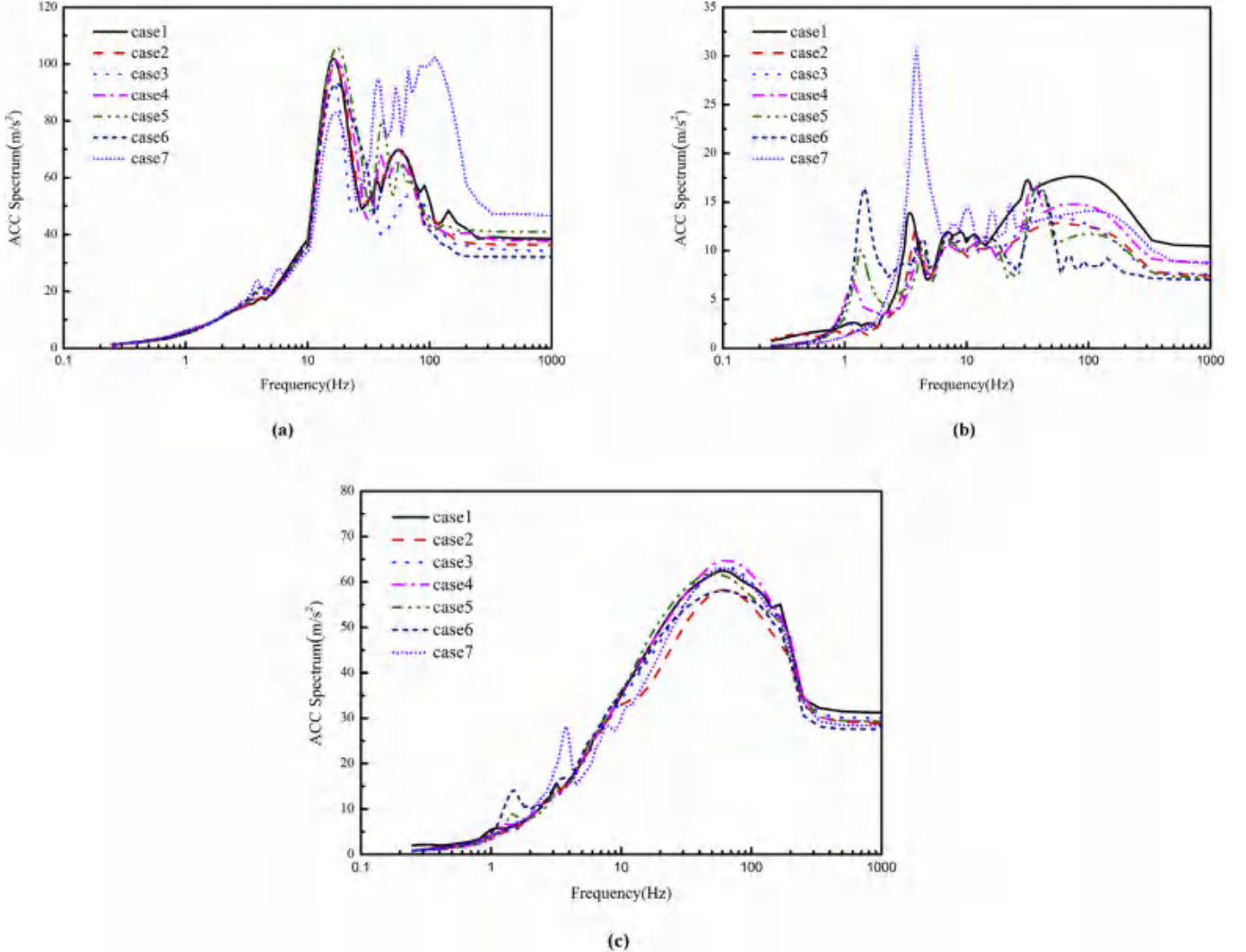


Fig. 24. The X acceleration spectra of the impact location central node under the impact of each aircraft load during the vibration attenuation process: (a) F4, (b) A320, and (c) 707-320.

instantaneous impact acceleration near the impact location.

Fig. 24 shows the X acceleration spectra for the central node of the impact location under different AI loads for the vibration attenuation process. It can be found that the acceleration spectrum varies for different AI loads. For the F4 load, there is little difference in the acceleration response spectrum at frequencies lower than 20 Hz, while there is a large difference after 20 Hz. For the A320 load, the peak value is between 1 Hz and 2 Hz for case 4 through case 6. There is a peak for all cases at approximately 4 Hz, and case 7 has the greatest peak value among all the cases. For the 707-320 load, the differences between the cases are not clear. Furthermore, the acceleration response for this process is smaller than that of the whole process.

Because the base mat is located far away from the center node of the impact location, the acceleration response for the whole analysis period is analyzed. Fig. 25 shows the X acceleration spectra of the base-mat location under different AI loads. Compared with the results of the center node of the impact location, the acceleration response of the base mat varies among the different cases. Under the different AI loads, there are some peak acceleration response spectrum values near specific frequencies. For the F4 load, there are

notable peaks near 1.5 Hz, 4 Hz, 15 Hz, and 45 Hz. For the A320 load, there are peaks near 1.5 Hz, 4 Hz, and 10 Hz. For the 707-320 load, there are clear peaks near 1.5 Hz, 4 Hz, 10 Hz, and 40 Hz. The maximum peak values of the acceleration response spectrum for case 1 through case 3 appear near 45 Hz, and the maximum peak values for case 4 to case 6 appear near 15 Hz. The peaks of the acceleration time history for case 1 through case 6 are similar: approximately  $8 \text{ m/s}^2$  under the F4 load,  $4 \text{ m/s}^2$  under the A320 load, and  $4 \text{ m/s}^2$  under the 707-320 load.

In Fig. 25, the X acceleration response spectrum of case 6 under the action of the El Centro seismic wave is considered. There is a clear difference between the acceleration response spectra of the structures under the earthquake load and those of the AI load. The frequency bandwidth of the acceleration response spectrum is larger for the AI load than that for the earthquake load. Under the earthquake load, the acceleration response spectrum of the structure has two peaks; one is near 4 Hz, and the other is near 10 Hz. For some aircraft loads, such as the F4 load, the high-frequency component of the acceleration response spectrum is notably higher than that under the earthquake load. The sensitivities of the different internal devices and instruments to the acceleration

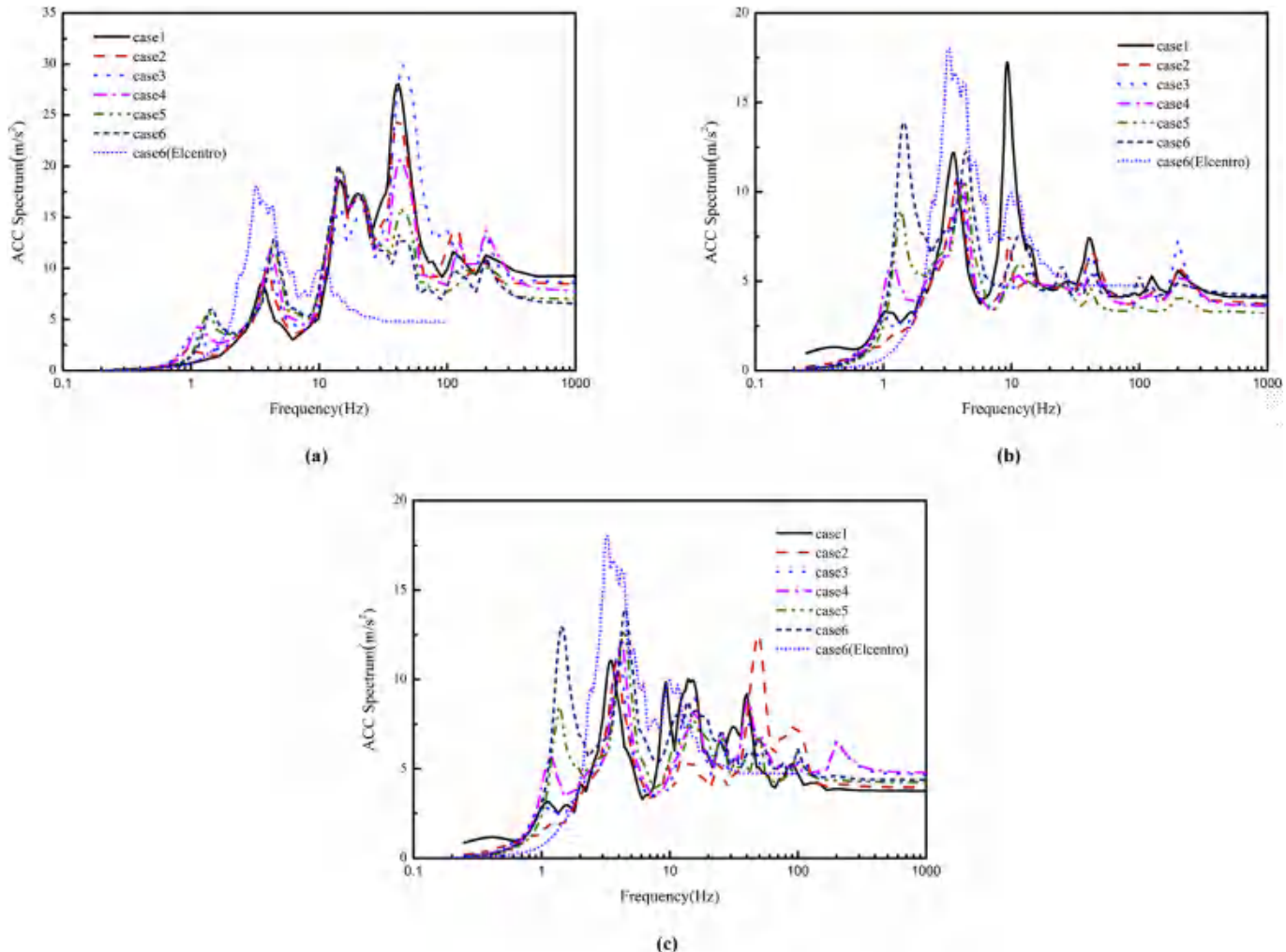


Fig. 25. Comparison of the acceleration spectra of the base-mat center node between the earthquake load and various AI loads: (a) F4, (b) A320, and (c) 707-320.

response in the different frequency regions vary; therefore, for the vibration safety of the equipment and instruments, the effects of the different loads require consideration.

## 5. Conclusions

The dynamic characteristics of base-isolated structures under different AI loads are analyzed for the CPR1000 NPP and are summarized in detail. The conclusions are as follows:

1. The flexible isolation layer between the base-mat and the foundation weakens the constraint function of the foundation on the superstructure. This can effectively reduce the seismic response of the superstructure. But under the AI loads, there will be adverse effects. Under a sufficiently large AI, the isolation bearings will cause considerable horizontal deformation. In serious cases, it can cause structural instability. In addition, the isolation bearing with different horizontal stiffness coefficient has obvious influence on the vibration response of the base-mat, such as the frequency component and the amplitude of the vibration response.
2. Under different AI loads, due to the short duration of AI load, the plastic strain area distribution of the containment is mainly distributed in the region local to the impact location. The

presence of an isolation system will not significantly affect the distribution of the containment plastic strain area.

3. The impact loads produced by different tonnage aircraft under different impact velocities have their own characteristics. Given the same isolation conditions, the displacement and acceleration responses of the containment vary owing to the different characteristics produced by the different AI loads.

## Acknowledgments

This research was supported by Grant 2016YFB0201000 from National Major Scientific Research Program of China, Grant 51421064 from the National Natural Science Foundation of China, DUT17LK16 from the Fundamental Research Funds for the Central Universities, and Grant 51409074 from the National Natural Science Foundation of China.

## Appendix A. Supplementary data

Supplementary data related to this article can be found at <https://doi.org/10.1016/j.net.2018.08.003>.

## References

- [1] 10CFR50.150, Aircraft Impact Assessment, 2009.

- [2] J.D. Riera, On the stress analysis of structures subjected to aircraft impact forces, *Nucl. Eng. Des.* 8 (1968) 415–426.
- [3] IAEA, Safety Aspects of Nuclear Power Plants against Human Induced External Events: Margin Assessment, Draft Safety Report DD1086, 2014.
- [4] J. Arros, N. Doumbalski, Analysis of aircraft impact to concrete structures, *Nucl. Eng. Des.* 237 (12) (2007) 1241–1249.
- [5] K. Lee, S.E. Han, J.W. Hong, Analysis of impact of large commercial aircraft on a prestressed containment building, *Nucl. Eng. Des.* 265 (6) (2013) 431–449.
- [6] M. Kostov, F.O. Henkel, A. Andonov, Safety assessment of A92 reactor building for large commercial aircraft crash, *Nucl. Eng. Des.* 269 (4) (2014) 262–267.
- [7] J. Hua, G.C. Mi, Aircraft impact analysis of nuclear safety-related concrete structures: a review, *Eng. Fail. Anal.* 46 (2014) 118–133.
- [8] S.S. Sang, D. Hahm, T. Park, Shock vibration and damage responses of primary auxiliary buildings from aircraft impact, *Nucl. Eng. Des.* 310 (2016) 57–68.
- [9] S.J. Jeon, B.M. Jin, Y.J. Kim, Assessment of the fire resistance of a nuclear power plant subjected to a large commercial aircraft crash, *Nucl. Eng. Des.* 247 (6) (2012) 112–122.
- [10] M.R. Sadique, M.A. Iqbal, A. Rawwas, et al., Response of outer containment of an NPP against aircraft crash and induced fire, *Thin-Walled Struct.* 126 (2018) 182–192.
- [11] G. Qian, M. Niffenegger, Integrity analysis of a reactor pressure vessel subjected to pressurized thermal shocks by considering constraint effect, *s112e113*, *Eng. Fract. Mech.* s112e113 (2013) 14e25.
- [12] V.F. González-Albuixech, G. Qian, M. Sharabi, et al., Integrity analysis of a reactor pressure vessel subjected to a realistic pressurized thermal shock considering the cooling plume and constraint effects, *Eng. Fract. Mech.* 162 (2016) 201–217.
- [13] A.S. Whittaker, M. Kumar, M. Kumar, Seismic isolation of nuclear power plants, *Nucl. Eng. Technol.* 46 (5) (2014) 569–580.
- [14] LS-DYNA, Keyword User's Manual, Revision 971, Liver more Software Technology Corporation, 2007.
- [15] C. Heckóter, A. Vepsä, Experimental investigation and numerical analyses of reinforced concrete structures subjected to external projectile impact, *Prog. Nucl. Energy* 84 (2015) 56–67.
- [16] X. Lu, K. Lin, S. Cen, et al., Comparing different fidelity models for the impact analysis of large commercial aircrafts on a containment building, *Eng. Fail. Anal.* 57 (2015) 254–269.
- [17] L.J. Malvar, J.E. Crawford, J.W. Wesevich, et al., A plasticity concrete material model for DYNA3D, *Int. J. Impact Eng.* 19 (9e10) (1997) 847–873.
- [18] Ping Yi, Qingkang Wang, Jun Liu, Research on failure mechanism of CPR1000 containment vessel under internal pressure, *J. Harbin Eng. Univ.* 37 (2) (2016) 162–167.
- [19] L.J. Malvar, C.A. Ross, Review of strain rate effects for concrete in tension, *ACI Mater. J.* 96 (5) (1999) 614–616.
- [20] P.H. Bischoff, S.H. Perry, Compressive behavior of concrete at high strain rate, *Mater. Structur.* 24 (1991) 425–450.
- [21] Jianwei Cao, Qin Fang, Ziming Gong, et al., Numerical investigation on response and damage of nuclear containments under aircraft impact, *Eng. Mech.* 31 (9) (2014) 63e70.
- [22] F. Sun, R. Pan, L. Wang, et al., Study on effective prestressing effects on concrete containment under the design-basis pressure condition, *Nucl. Saf.* 12 (3) (2013) 20e25.
- [23] K. Muto, H. Tachikawa, T. Sugano, H. Kobayashi, Y. Kasai, N. Koshika, T. Tsujimoto, Experiment studies on local damage of reinforced concrete structures by the impact deformable missiles - part 1: outline of test program and small-scale tests, in: *Transactions of 10th International Conference on Structural Mechanics in Reactor Technology*, August 14–19, California, 1989.
- [24] M. Kumar, A.S. Whittaker, M.C. Constantinou, An advanced numerical model of elastomeric seismic isolation bearings, *Earthq. Eng. Struct. Dynam.* 43 (13) (2015) 1955–1974.
- [25] M. Kumar, A.S. Whittaker, M.C. Constantinou, Experimental investigation of cavitation in elastomeric seismic isolation bearings, *Eng. Struct.* 101 (2015) 290–305.
- [26] R.L. Frano, G. Forasassi, Isolation systems influence in the seismic loading propagation analysis applied to an innovative near term reactor, *Nucl. Eng. Des.* 240 (10) (2010) 3539–3549.
- [27] J. Chen, C. Zhao, Q. Xu, et al., Seismic analysis and evaluation of the base isolation system in AP1000 NI under SSE loading, *Nucl. Eng. Des.* 278 (2014) 117–133.
- [28] Z. Zhou, J. Wong, S. Mahin, Potentiality of using vertical and three-dimensional isolation systems in nuclear structures, *Nucl. Eng. Technol.* 48 (5) (2016) 1237e1251.
- [29] C. Rouzaud, F. Gatuingt, G. Hervé, et al., Influence of the aircraft crash induced local nonlinearities on the overall dynamic response of a RC structure through a parametric study[J], *Nucl. Eng. Des.* 298 (2016) 168–182.
- [30] A. Andonov, M. Kostov, A. Iliev, Capacity assessment of concrete containment vessels subjected to aircraft impact, *Nucl. Eng. Des.* 295 (2015) 767–781.
- [31] H. Abbas, D.K. Paul, P.N. Godbole, G.C. Nayak, Aircraft crash upon outer containment of nuclear power plant, *Nucl. Eng. Des.* 160 (1996) 13e50.
- [32] M.A. Iqbal, S. Rai, M.R. Sadique, et al., Numerical simulation of aircraft crash on nuclear containment structure, *Nucl. Eng. Des.* 243 (2012) 321–335.
- [33] M.R. Sadique, M.A. Iqbal, P. Bhargava, Nuclear containment structure subjected to commercial and fighter aircraft crash, *Nucl. Eng. Des.* 260 (2013) 30–46.
- [34] M.A. Iqbal, M.R. Sadique, P. Bhargava, et al., Damage assessment of nuclear containment against aircraft crash, *Nucl. Eng. Des.* 278 (8) (2014) 586–600.
- [35] D.K. Thai, S.E. Kim, Safety assessment of a nuclear power plant building subjected to an aircraft crash, *Nucl. Eng. Des.* 293 (November 2015) (2015) 38–52.
- [36] Nuclear Energy Institute (NEI 07-13 Rev. 8), Methodology for Performing Aircraft Impact Assessments for New Plant Designs, 2011.